Contents lists available at ScienceDirect

Transactions of Nonferrous Metals Society of China

36(2026) 538−551

www.tnmsc.cn

Effect of sintering temperature on microstructure and mechanical properties of 95W-HEA alloys

Shi-dong XIE, Liang-liang TANG, Bo-hua DUAN*, Zhuang-zhi WU, De-zhi WANG

School of Materials Science and Engineering, Central South University, Changsha 410083, China

Abstract: The use of high entropy alloy as a binder for tungsten heavy alloys offers potential advantages. The 95W-5CoCrFeMnNi alloys (95W-HEAs) were prepared via powder metallurgy at sintering temperatures of 1400−1550 °C. The microstructure analysis revealed that the tungsten phase in 95W-HEAs exhibited a nearly spherical morphology in the HEA binder matrix and the formation of a Cr−Mn oxide mixed phase was observed. The sintering temperature exerted a significant influence on the relative density, grain size, W−W contiguity, and mechanical properties of the alloys. The optimal performance was achieved when sintering at 1450 °C, yielding a relative density of 96.61%, a W−W contiguity of 0.528, an average grain size of 18.97 μm, a compressive strength of 2234.82 MPa, and a hardness of HV 400.6. The activation energy for the diffusion of tungsten in the liquid phase formed by HEA binder was calculated to be 354.514 kJ/mol, highlighting its role in controlling grain growth.

Keywords: tungsten heavy alloys; high entropy alloy binder; sintering temperature; densification; mechanical properties

1 Introduction

Tungsten heavy alloys (WHAs) are widely used in aerospace, military weapons, and medical devices due to their high density, superior strength and plasticity, excellent corrosion resistance, and good radiation shielding properties [1−3]. WHAs are typically fabricated by liquid-phase sintering (LPS) of tungsten with a blend of transition metals, resulting in tungsten grains with a body-centered cubic (BCC) structure dispersed in a face-centered cubic (FCC) binder network [4]. Conventional binders including Ni−Fe, Ni−Cu, Ni−Fe−Co, and Ni−Fe−Mo are commonly used in WHAs [5]. However, these binders exhibit limitations such as poor corrosion resistance and self-sharpening [6,7]. To solve these problems and enhance the overall performance of WHAs, alloying elements like Mn and Cr are often introduced. Nevertheless, this can lead to oxidation issues and render the sintering process control more intricate [8,9]. Therefore, the development of a novel binder phase for WHAs is imperative.

Recently, there has been a growing interest in high entropy alloys (HEA) due to their unique phenomena, such as high entropy effect, lattice distortion effect, sluggish diffusion effect, and cocktail effect [10]. As a result, they exhibit a good balance between strength and plasticity, high temperature stability, and thermal shock resistance, which have generated increasing scholarly attention and a constant expansion of their application fields [11]. Currently, HEA has been gradually applied as a binder or reinforcement phase in copper-based, magnesium-based, WC, and other materials [12]. And, they also show promise as potential binder materials for WHAs.

JIAN et al [13] and ZHOU et al [14] developed an $Al_{0.5}Cr_{0.9}FeNi_{2.5}V_{0.2}$ HEA as a binder phase for

Corresponding author: *Bo-hua DUAN, Tel: +86-18900744955, E-mail: duan-bh@csu.edu.cn

https://doi.org/10.1016/S1003-6326(25)66980-9

Received 25 May 2024; accepted 14 September 2024

WHAs. They investigated the wettability between two different phases and the effect of HEA on tungsten grain growth behavior. The system exhibited a low contact angle during liquid-phase sintering, and tungsten had a high solubility in HEA, which was beneficial for the densification process in LPS and contributed to high HEA/W interface bonding strength. Due to the low diffusion performance of high entropy alloys, the calculated grain growth constant was significantly lower than that of traditional binder phases, and an ultimate tensile strength up to 1267.3 MPa can be achieved when sintered at 1500 °C. A series of subsequent treatments such as solid solution strengthening, forging, and aging performed on sintered W-HEA alloys resulted in the formation of unique precipitates within the alloy system. These microstructural modifications improved the dynamic yield strength of the alloy and generated a narrow adiabatic shear band with high magnetization, which promoted self-sharpening behavior. In addition, the Cantor family of high entropy alloys composed of transition metals has garnered significant attraction as binder phases for WHAs due to their similar elemental composition to traditional binder phases. And, the Cantor alloys with single FCC structure have presented excellent room temperature performance and corrosion resistance. PANIGRAHI et al [15] prepared a FeNiCoCrCu HEA powder by mechanically milling elemental powders of Fe, Ni, Co, Cr, and Cu, and used it as a binder to obtain a 90W-HEAs via LPS. The resulting WHAs presented relatively higher density, hardness, and compressive strength. Likewise, LI et al [16] manufactured a novel fine-grained W−5Mo-7CoCrFeMnNi-1La_2O_3 composite material, investigated the microstructures and strengthening effects of added substances, and then explained the reasons for the ultra-high compressive strength and hardness of the composite material. In their study, the prepared WHAs showed a significant improvement in corrosion resistance, with an order of magnitude decrease in corrosion current and a half fall in corrosion voltage compared to traditional binders.

Despite the promising results, some challenges remain in replacing traditional binders with HEAs, including inadequate density, poor plasticity, and enrichment of partial element oxidation. To address these issues, some new preparation processes or techniques, such as additive manufacturing [17], microwave sintering [18], and spark plasma sintering (SPS) [19] were explored. SATYANARAYANA et al [20] fabricated 93WHEAs using CoCrFeMnNi as a binder with different sintering methods. They demonstrated that SPS with a higher heating rate and shorter sintering time can effectively reduce the volume fraction of Cr−Mn oxide and obtain higher compressive strength. Although advanced methods are effective, traditional powder metallurgy methods continue to dominant due to their operational ease, batch production capabilities, and cost-effectiveness [21]. So far, although a little research work has been carried out in the preparation of W-HEA alloys, there is still a significant lack of research in the systematic design of high entropy alloy composition, sintering densification mechanism, and sintering kinetics for W-HEA alloys. Especially, the systems studied in other works typically have a tungsten content of about 90%, and the research on W-HEA alloys with high W content is almost blank.

To obtain a higher density alloy, the 95W-5CoCrFeMnNi (wt.%) is prepared by the traditional powder metallurgy method. This work aims to investigate the effect of different sintering temperatures on the microstructure and mechanical properties of 95W-HEA alloys. Here, HEA binder is used in WHAs with high tungsten content, the relative density, contiguity, and dihedral angle of WHEAs at different temperatures were characterized to research the grain growth and densification behavior in detail, and the sintering temperature for optimal performance was also explored.

2 Experimental

2.1 Material preparation

The tungsten powder (purity of 99.9%, Xiamen Tungsten Industry Corporation, China) by the reduction method and the CoCrFeMnNi high entropy alloy powder (purity of 99.9%, Yijin New Material Corporation, China) by the gas atomization were employed as raw materials. Figures 1(a, b) depict the micrographs of tungsten powder and HEA powder, respectively. The tungsten powder exhibits a granular morphology with particle sizes ranging 1−2 μm, while the high entropy alloy powder assumes a spherical shape with particle sizes of 1−25 μm, as confirmed by merchant information and SEM images. In addition, Fig. 1(c) reveals that the high entropy alloy system has an FCC structure.

According to the calculated results of LI et al [16], the values of parameters $\Omega(=T_m\Delta S_{mix}/|\Delta H_{mix}|)$, δ (atomic size difference of elements) and VEC (valence electron concentration) in the equiatomic CoCrFeMnNi alloy are 5.77, 0.92, and 8.0, respectively. This system is capable of forming stable and disordered solid solutions in FCC phase, which aligns with the results of CATOR et al [22], YANG and ZHANG [23] and GUO et al [24].

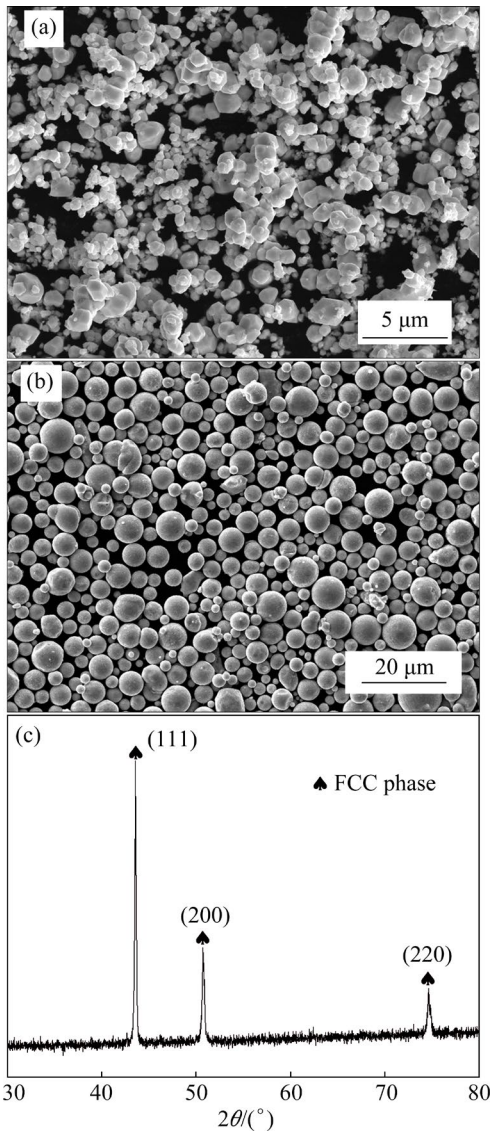

Fig. 1 SEM images of (a) W powder and (b) HEA powder; (c) XRD pattern of HEA powder

The powder mixture of tungsten and high entropy alloy, with a mass ratio of 95∶5, was blended for 10 h at a speed of 120 r/min with a ball to material ratio of 1∶1 in an argon atmosphere on a pot mill (GMS5−2, Changsha Miqi, China). The resulting mixed powder was then placed into a rectangular mould and subjected to a uniaxial pressure of 200 MPa for 120 s to produce green compacts with an approximate size of 42 mm× 15 mm×7 mm. The green compacts present a density of about 9.4 g/cm^3 and a relative density of about 52.0%. Finally, the green compacts were sintered in a high-temperature hydrogen tubular furnace (KSL−1700X, Hefei Kejing, China). The sintering procedure involved holding at 800 °C for 60 min to reduce the oxidation of the powder, followed by sintering at 1400, 1450, 1500, and 1550 °C for 90 min, respectively. The heating or cooling rate is 10 °C/min and 5 °C/min before and after 1000 °C, but furnace cooling below 700 °C. To prevent powder oxidation, the continuous flow of hydrogen with a purity of 99.99% and a dew point lower than −50 °C was applied to purging the tube during sintering.

2.2 Characterization and performance testing

A high-precision density meter (DE−120M, Dongguan Hongtuo, China) was used to measure the actual density (ρ_t) of the samples and the relative density ($\rho_t/\rho_0\times100\%$). The theoretical density (ρ_0) of the alloy is derived from Eq. (1) [7]:

$$\rho_0=1/\sum\left(x_i/\rho_i\right) \tag{1}$$

where x_i is the mass fraction of each component in the alloy, and ρ_i is the theoretical density of each component. The actual density of CoCrFeMnNi high entropy alloy is 8.018 g/cm^3 based on test measurement and theoretical calculation. Phase analysis of tungsten heavy alloy samples was conducted using an X-ray diffractometer (D/Max2500, Rigaku, Japan) with a scanning angle (2θ) of 30°−80° and a scanning speed of 5 (°)/min, using Cu K_α radiation (λ=1.54 Å). Scanning electron microscopy (SEM, Mira4, Tescan, Czech Republic) equipped with an energy dispersive spectrometer (EDS, Xplore30, Aztecone, Oxford) was employed to observe the microstructure and element distribution of sintered samples. The obtained micrographs were used to statistically evaluate grain size, tungsten contiguity (C_W), and tungsten solid volume fraction (V_S) at various sintering temperatures. C_W is calculated according to Eq. (2):

$$C_W=\frac{2N_{W-W}}{2N_{W-W}+N_{W-M}} \tag{2}$$

where N_{W-W} and N_{W-M} are the numbers of interface for W−W and W−binder matrix, respectively,

determined by the line intercept method [25]. This involved placing gridlines on the SEM images and counting the number of contact points, with an average of at least 80 measurements taken. The grain size and V_s were obtained after treating with the software of Image J.

The hardness (HV) of the sintered specimen was measured using a Vickers hardness tester (HVS−1000, Shanghai Lianer, China). At this time, 1 kg load was applied on the samples and held for 10 s, and the average value was obtained after selecting 8 different points. The sintered samples were machined into cylindrical shapes of d4 mm × 6 mm and then tested for compressive behavior on an electronic universal testing machine (DDL300, Changchun Zhongji, China), at a compression rate of 0.5 mm/min.

3 Results and discussion

3.1 Phase constitution and microstructure

Figure 2 shows the XRD patterns of the 95W-HEA alloys prepared at varying sintering temperatures. It can be seen that the main characteristic peaks corresponding to the tungsten phase of BCC are obvious, while the peak corresponding to the γ(W,Ni,Fe,Co) phase is also observed. The peak position of the γ phase shifts compared to Fig. 1(c), which may be attributed to the oxidation of chromium and manganese in HEA and the dissolution of W in the binder phase. Such component transitions and low mass fraction of binder are the reasons why other peaks in the FCC are difficult to observe. Simultaneously, the characteristic peaks corresponding to Cr−Mn oxidation phase are also displayed. The oxide phase has been reported in the preparation of almost all high entropy alloys containing Cr or Mn elements via powder metallurgy [20,26]. The formation of oxide phase may deteriorate the performance of the W-HEA alloys, suggesting that the addition of Cr or Mn elements in the design of HEA binder for WHAs should be avoided or significantly reduced.

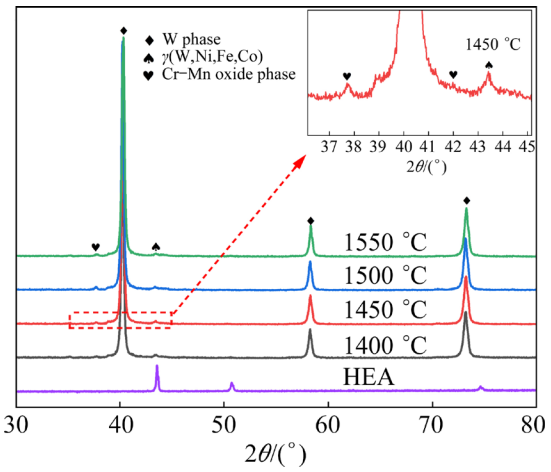

Fig. 2 XRD patterns of 95W-HEA samples sintered at different temperatures

Figure 3 presents the SEM images of 95W-HEA alloys sintered at different temperatures. The microstructure of the 95W-HEA alloys consists of several regions with different colors, including bright, gray, irregular black, and small black spots. To identify the phase composition of each region, the elemental distribution mappings and energy dispersive spectrometer (EDS) analysis were performed on the 95W-HEA specimen sintered at 1450−1550 °C, and the results are shown in Fig. 4. Combined with the XRD patterns in Fig. 2, it can be inferred that the bright region, gray region, and irregular black region marked in Fig. 3(b) correspond to the spherical tungsten grains, the γ(W,Ni,Fe,Co) binder phase, and the Cr−Mn composite oxide phase, respectively, while the small black dots represent the residual pores after sintering. Each phase at different temperatures appears and presents a very similar phase element composition, which means that these phases exist stably in this temperature range. Therefore, the 95W-HEA alloys comprise three distinct phases: a bright W phase, a gray γ(W,Ni,Fe,Co) binder phase, and a dark mixed Cr−Mn oxide phase, which is consistent with the findings of related reports [20].

Based on the research reports, the CoCrFeMnNi HEA powder utilized in this study possesses a melting point of 1334 °C [27]. Consequently, the microstructure of the 95W-HEA alloys obtained under the experimental conditions exhibits a typical liquid-phase sintered microstructure, characterized by near-spherical W grains uniformly embedded in a soft matrix phase. Compared to traditional WHAs, the microstructure of the 95W-HEA alloys becomes more complex due to the use of the HEA binder phase containing multiple elements.

Figure 4 shows the elemental distribution mappings of samples sintered at 1450−1550 °C and the EDS spot analysis result of sample sintered at 1450 °C. During the high-temperature sintering process, W would diffuse and dissolve with the

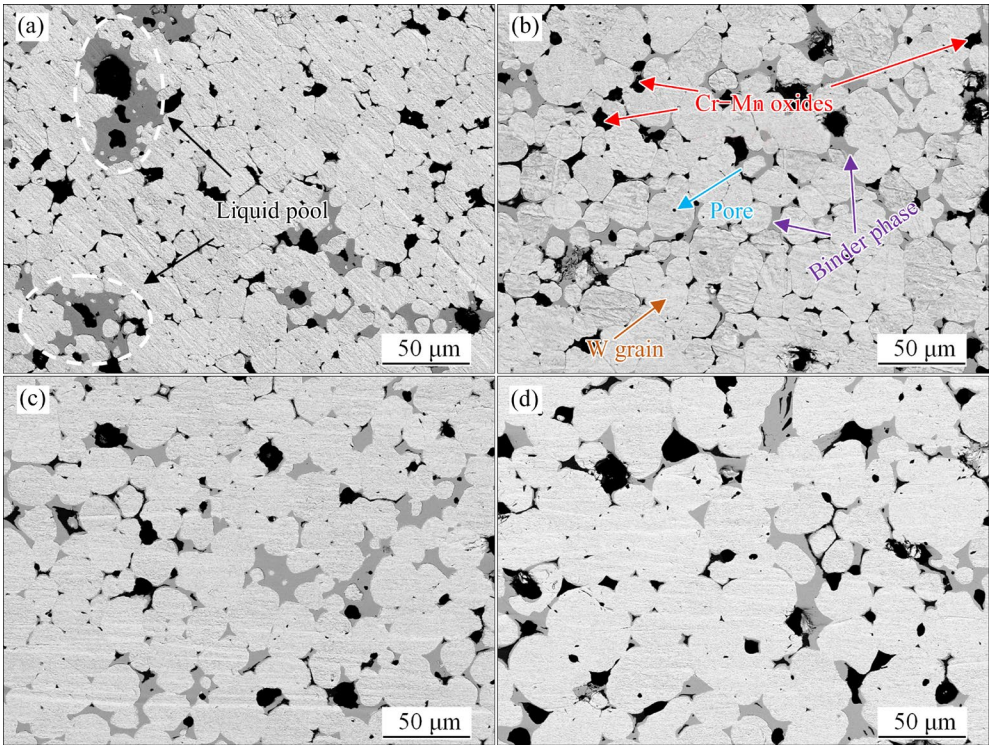

Fig. 3 SEM images of 95W-HEA samples sintered at different temperatures: (a) 1400 °C; (b) 1450 °C; (c) 1500 °C; (d) 1550 °C

various components in the HEA, leading to a change in the composition of the binder phase, as confirmed in Table 1. W is soluble in the HEA binder and vice versa, the mutual solubility phenomenon not only enhances the wettability between tungsten and the binder HEA phase, but also increases the quantity of the liquid phase, thereby accelerating densification of the W-HEA alloys and strongly affecting the grain growth of W [28]. Meanwhile, the presence of oxygen, which is inevitably derived from the raw powders or introduced during the preparation process, further complicates the situation. Oxygen can dissolve in both the W phase and the binder phase, and also be prone to form stable oxide phases with Cr and Mn atoms in the HEA at the interface between W and the binder phase, as they manifest a lower Gibbs free energy change value than other elements [16]. The oxide phases of chromium and manganese are difficult to reduce and almost insoluble with W, which can weaken the interfacial binding strength, resulting in a decline in the performance of the WHAs. On the other hand, the oxide layer formed on the surface of tungsten particles isolates the contact between tungsten and the binder phase, thereby hindering the dissolution and precipitation of W in the binder phase, which is not conducive to densification. This is supported by the lower W content of the gray phase in Spot 3# compared to that of the gray phase in Spot 2#. Consequently, when the binder phase used contains a high concentration of chromium or manganese elements, controlling oxygen content during the preparation is critical for the WHAs to achieve optimal properties.

In addition, the sintering temperature also has a significant impact on the microstructure of 95W-HEA alloys. An increase in sintering temperature results in the growth of W grains and exacerbated oxidation; however, it can also improve the homogeneity of the structure (Fig. 3). At 1400 °C, the binder forms the “isolated liquid pool” within the alloy, causing numerous tungsten grains to aggregate closely together, even exhibiting some solid-phase sintering characteristics. The low amount and the high viscosity of liquid phases formed at 1400 °C, near the melting point, may be responsible for this phenomenon. As the temperature rises to 1450 °C or 1500 °C, the amount of liquid phase increases, and its viscosity decreases. This facilitates the flow of the liquid phase among particles and the filling of large isolated pores, contributing to rapid rearrangement and uniform distribution of W particles in the binder

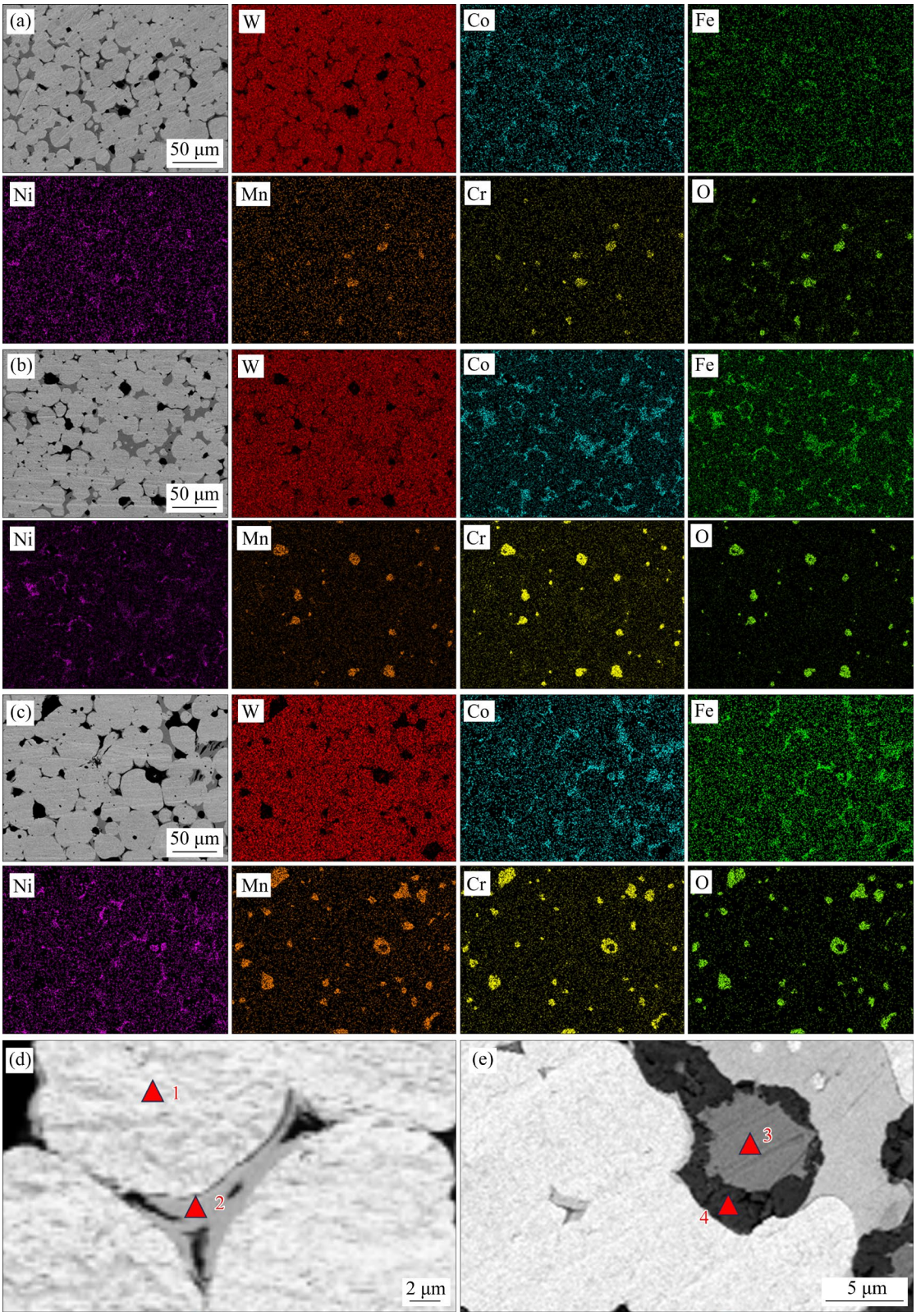

Fig. 4 Elemental distribution mappings of 95W-HEA samples sintered at (a) 1450 °C, (b) 1500 °C and (c) 1550 °C; (d, e) EDS spot analysis of sample sintered at 1450 °C

phase. However, if the sintering temperature further increases to 1550 °C, the W grains grow significantly, caused by the accelerated dissolution and the precipitation of W in HEA at high temperatures, which may deteriorate the mechanical properties of the W-HEA alloys.

3.2 Densification and grain growth

During the liquid-phase sintering process, the densification can be divided into three stages [5]: (1) the formation of the liquid phase and the rearrangement of tungsten particles; (2) dissolution−reprecipitation of the tungsten in binder phase (at this stage, the intergranular film rich in nickel may act as a preferential diffusion pathway [29,30]); (3) the formation of a tungsten solid phase skeleton. The close contact of solid particles hinders rearrangement, and the remaining liquid phase fills the gaps in the skeleton, thus completing the sintering process. Table 2 gives the relative density, the volume fraction of W, contiguity, and the dihedral angle of 95W-HEA alloys sintered at different temperatures. The relative density of the 95W-HEA alloys slightly increases with temperature, ranging from 95.61% to 97.27%, which is a little higher than the value (95.70%) reported for 90W-HEA alloy by PANIGRAHI et al [15], but lower than that of traditional WHAs [31]. In liquid-phase sintering, the density of alloys is typically influenced by factors such as liquid phase volume and viscosity, tungsten content, and particle wettability. While previous studies have demonstrated easy densification of WHAs with low tungsten content [32], the high tungsten content in the alloy limits the production of a sufficient liquid phase to fully contact particles. This hinders the rearrangement and leads to incomplete densification. In addition, there are voids or non-wettability between the Cr−Mn oxidation and the binder phase. The above factors contribute to the low density in this study. In general, increasing sintering temperature promotes liquid content, reduces viscosity, and enhances atomic diffusion. However, these positive effects may be counterbalanced by the low diffusion kinetics of high entropy alloys and the formation of oxide phases on the tungsten surface. These factors explain the observed trend in relative density.

Table 1 Element compositions of different positions in 95W-HEA samples (at.%)

Sintering temperature/°C	Position	O	Cr	Mn	Fe	Co	Ni	W
1450	W grain (Spot 1# in Fig. 4(d))	5.72±0.83	1.17±0.77	0.00±0.00	0.40±0.08	0.22±0.11	0.31±0.18	92.18±1.03
	Binder (Spot 2# in Fig. 4(d))	10.62±1.38	3.06±0.93	2.84±0.46	15.21±1.00	18.64±0.93	10.61±1.00	39.02±1.80
	Oxide-enclosed binder (Spot 3# in Fig. 4(e))	5.13±0.21	4.03±1.24	9.64±3.43	21.37±1.59	21.66±2.52	29.82±0.63	8.37±0.98
	Oxides (Spot 4# in Fig. 4(e))	58.26±0.87	27.26±0.86	13.73±0.51	0.12±0.11	0.10±0.08	0.12±0.09	0.41±0.26
1500	W grain	7.19±1.46	1.14±0.18	0.38±0.12	0.89±0.32	0.16±0.04	0.13±0.02	90.11±1.89
	Binder	12.84±1.36	3.41±1.10	1.24±0.19	13.36±1.89	17.23±1.23	11.43±0.12	40.49±1.68
	Oxides	54.69±4.09	29.62±2.41	15.24±1.72	0.05±0.04	0.08±0.06	0.03±0.01	0.29±0.04
1550	W grain	8.19±3.57	0.75±0.20	0.17±0.26	0.51±0.11	0.43±0.26	0.03±0.01	89.92±3.69
	Binder	11.34±3.36	2.01±1.17	0.75±0.32	14.62±1.38	16.78±1.87	12.66±1.20	41.84±0.85
	Oxides	59.60±2.64	26.14±1.66	13.72±1.31	0.12±0.02	0.07±0.01	0.06±0.05	0.29±0.08

Table 2 Relative density, volume fraction of W-solid (V_S), contiguity (C_W) and dihedral angle (φ) of 95W-HEA samples sintered at different temperatures

Sintering temperature/°C	Relative density/%	V_S/%	C_W	φ/(°)
1400	95.61±1.16	84.69±2.50	0.657±0.087	70.29±12.54
1450	96.61±0.20	83.26±1.70	0.528±0.086	65.89±9.84
1500	96.71±1.09	83.33±2.02	0.554±0.100	63.64±9.08
1550	97.27±0.24	84.00±0.76	0.562±0.117	62.99±13.12

On the other hand, the sintering temperature also influences the volume fraction of tungsten, contiguity of tungsten, and dihedral angle. The solid volume fraction of tungsten initially decreases with rising sintering temperature due to enhanced tungsten dissolution into the binder phase. However, the formation of oxide phase at high temperatures can impede dissolution and diffusion of tungsten, modifying the distribution of W in each phase, and thus changing the trend of the solid fraction. Additionally, the contiguity of tungsten (C_W) exhibits a similar variation trend to the volume fraction. At 1400 °C, the C_W is significantly higher compared to that at other temperatures due to the aggregation of tungsten grains (as shown in Fig. 3(a)). As the temperature increases, the distribution of each phase becomes more uniform, resulting in a decline in C_W. The subsequent slight increase may be attributed to grain growth, giving rise to a slight increase in the number of tungsten contact interfaces. The obtained C_W values range from 0.55 to 0.66. It is essential to prevent the deformation of 95W-HEA alloys during liquid-phase sintering [33].

The dihedral angle (φ) is calculated from Eq. (3) [34] using the values given in Table 2:

$$C_W = V_S^2\left(0.43\sin\varphi + 0.35\sin^2\varphi\right) \quad (3)$$

The dihedral angle is a crucial indicator of the wettability between liquid and solid particles. A smaller dihedral angle indicates greater favorability for sintering. It can be observed that the dihedral angle reduces as the temperature increases. This means that higher temperatures make the sintering of WHEAs easier, which conforms to the general principles of powder metallurgy. However, when compared to traditional binders like Ni−Fe [25,35], W-HEA alloys demonstrate higher values of C_W and φ, which are closely linked to the unique properties of the CoCrFeMnNi HEA used with low nickel content and low wettability for tungsten particles in the experiment.

Figure 5 shows the grain size distribution and the average size of 95-HEA alloys sintered at different temperatures. It can be seen that the grain size follows a normal distribution and the average size grows from 15.54 to 31.09 μm with rising temperature. The degree of growth is more pronounced at higher temperatures. Grain growth is a specific manifestation of the second stage of densification, which is a diffusion-controlled process that can be analyzed based on the Oswald ripening model. The grain growth behavior at this time can be mathematically expressed by Eqs. (4)−(8) [36,37]:

$$G^3 = G_0^3 + Kt \quad (4)$$

where G_0 and G are the grain sizes at the beginning of grain coarsening (t=0) and after sintering for a specific time t, respectively.

The parameter K is related to the material constants:

$$K = \frac{gD_S CVS}{kT\left(1-V_S\right)^{1/3}} \quad (5)$$

where g is the geometric constant, D_S represents the diffusivity of W in the liquid, C is the solubility of solids in the liquid phase, V is the atomic volume, S represents solid−liquid interface energy, k is the Boltzmann's constant, and T is the thermodynamic temperature.

D_S is relevant to temperature by Arrhenius' law as

$$D_S = D_0\exp[-Q/(RT)] \quad (6)$$

where D_0 is the pre-exponential factor, Q is the activation energy for the diffusion process, and R is the molar gas constant.

The parameters in Eq. (5) are not much affected by temperature except D_S, which implies that K in Eq. (4) exhibits a temperature dependence related to D_S, so K could be equal to

$$K = K_0\exp[-Q/(RT)] \quad (7)$$

where K_0 is the pre-exponential factor. Then, substitute Eq. (7) into Eq. (4) and take the natural logarithm on both sides as follows:

$$\ln(G^3 - G_0^3) = \ln K_0 + \ln t - Q/(RT) \quad (8)$$

The above equation (Eq. (8)) indicates that for a constant total time and activation energy Q, $\ln(G^3 - G_0^3)$ exists a linear relationship with $1/T$. The curve with r^2=0.9913 in Fig. 5(f) is fitted based on the average grain size G_A from Fig. 5(e) at each temperature, by assuming G_0=5 μm. The calculated activation energy (Q) for tungsten grain growth in this system is 354.514 kJ/mol, which is similar to that for the CoCuFeNi binder calculated by MA et al [38] and much higher than 113−162 kJ/mol of traditional Ni−Co and 106 kJ/mol of Ni−Fe [37]. This high activation energy may stem from the lattice

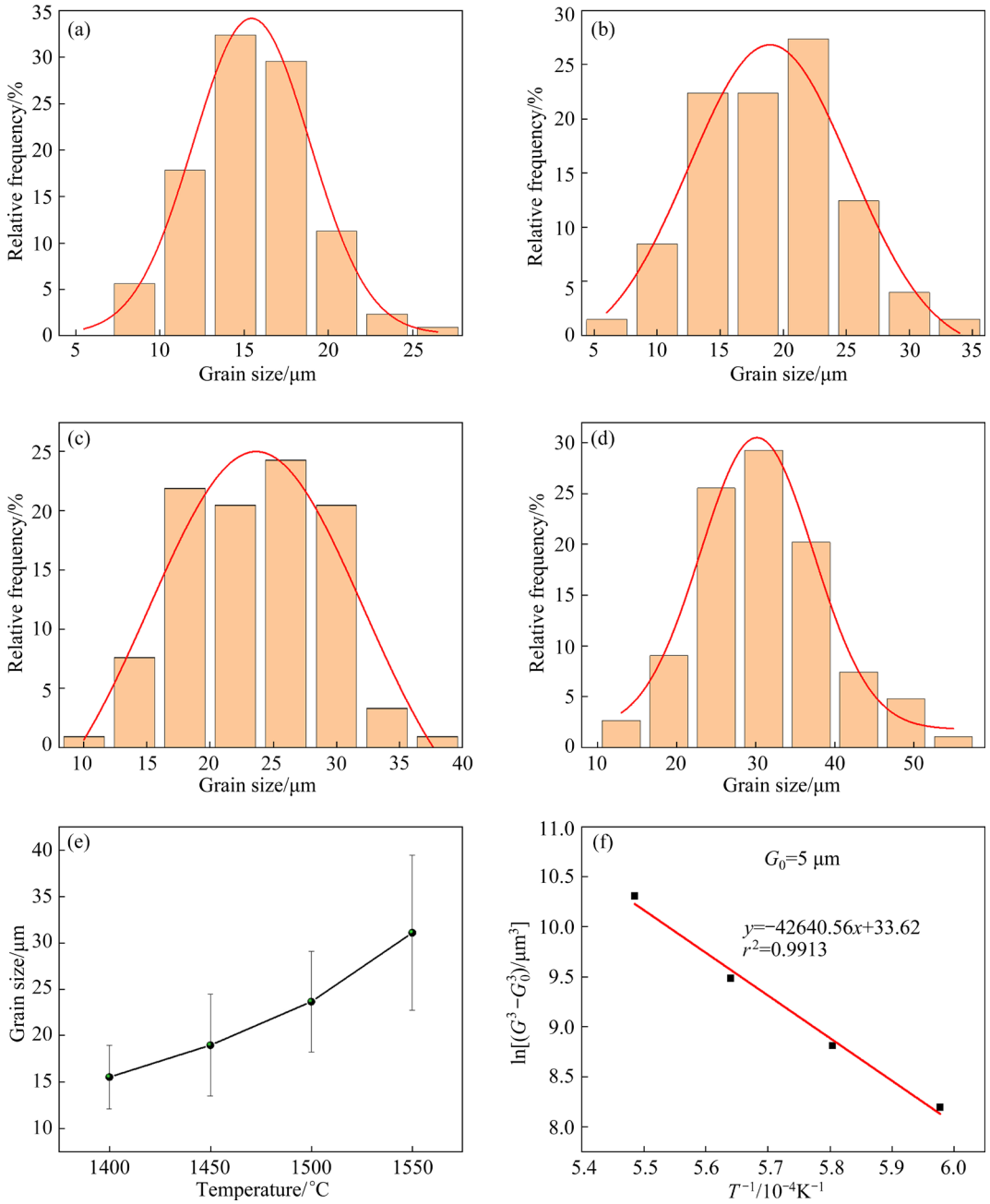

Fig. 5 Grain size distribution of 95W-HEA alloys sintered at (a) 1400 °C, (b) 1450 °C, (c) 1500 °C, and (d) 1550 °C; (e) Trend of average grain size change; (f) Fitting curve for activation energy calculation

distortion and slow diffusion of HEA, as well as the distribution of Cr−Mn oxide at the interface in the alloy, which greatly slows down the mass transfer and diffusion rate of tungsten in the liquid phase, requiring higher activation energy to facilitate the diffusion process. Furthermore, the cases where G_0 is equal to 3 and 8 μm are also considered. The calculated Q values are 371.307 kJ/mol and 350.572 kJ/mol, respectively. These results suggest that the value of G_0 does not exert a significant impact on Q, and therefore, the results are reliable.

3.3 Mechanical properties

Figure 6 shows compressive stress−strain curves of the samples and their compressive strength and fracture strain. The compression curves of the 95W-HEA alloys exhibit behavior consistent with brittle materials. This observation can be attributed to the high tungsten content and uneven phase distribution, which hinders the manifestation of yield phenomena. According to Fig. 6(b), the compressive strength and fracture strain of the alloy reach their peak at 1450 °C, attaining optimal performance

with 2234.82 MPa and 46.68%, respectively, before experiencing a decline. It is widely acknowledged that the mechanical properties of WHAs are heavily influenced by various factors, including tungsten content, relative density, grain size, W−W contiguity, microstructure composition, and uniformity. The sintering temperature plays a crucial role in determining these factors. Based on the results presented above, it is evident that the 95W-HEA alloy sintered at 1450 °C offers superior attributes in terms of density, W−W contiguity, grain size and distribution, and oxide phase content. The decrease in properties at 1400 °C is caused by the lower relative density and inhomogeneity of the microstructure. The attenuated performance after 1450 °C is primarily caused by the effect of grain growth and increased oxide phases on the interface between the tungsten and the binder phase.

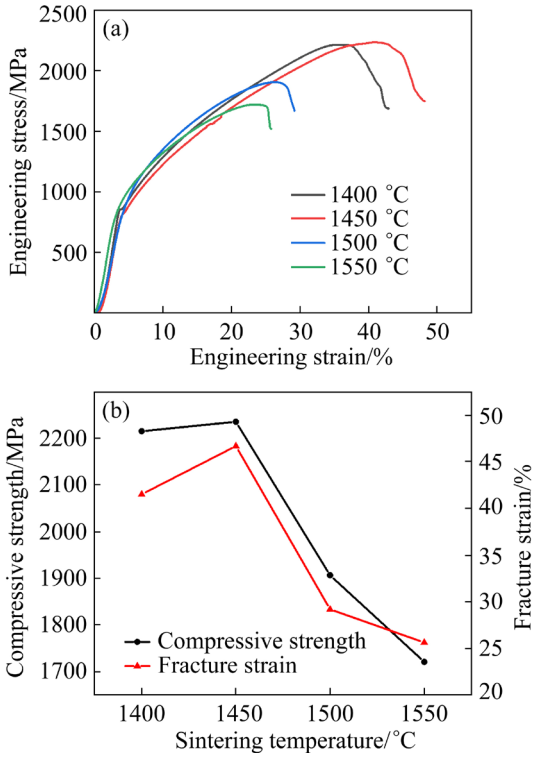

Fig. 6 Mechanical properties from compressive tests of 95W-HEA alloys: (a) Compression curve; (b) Compressive strength and fracture strain

The excellent properties obtained at 1450 °C can be attributed to the following mechanism. The alloy presents a smaller grain size and minimal C_W value at this temperature. According to the Hall−Petch equation modified by LEE et al [39], the reduction in grain size is conducive to enhancing the yield strength of alloy. The formation of fine grains is primarily attributable to the slow diffusion effect of HEA and the high activation energy of growth, which impedes grain growth and enhances performance. Secondly, the second phase Cr−Mn oxide generated in the alloy can hinder the mass transfer process in the tungsten precipitation−dissolution stage of the alloy, which has a positive effect on the grain size reduction. On the other hand, the two-phase interface and the softer FCC binder are the primary agents responsible for plasticity improvement. A small C_W indicates that there are more W−binder interfaces in the alloy. In this dual-phase composite alloy, the increase of the two-phase interface and the refinement of the grain are conducive to improving the storage capacity of the dislocation [40]. In addition, The dissolution of tungsten in the binder effectively enhances the comprehensive performance of binder, thereby facilitating a superior fit between tungsten and the binder. Therefore, the motion of the dislocation between the two phases can be facilitated, and the tungsten particles cannot be unglued prematurely, thus improving strength and plasticity.

Figure 7 illustrates the fracture morphology of the alloys sintered at 1400−1550 °C. The detachment of the W−binder, W−W interface, tearing of the binder, and a minor degree of tungsten cleavage are observable. Compression tests reveal that the deformation of this composite heterostructure alloy involves several processes [41]. Initially, the harder tungsten phase and the softer binder undergo elastic deformation. With increasing the deformation, the binder phase transitions to plastic deformation while the tungsten phase remains elastic. At this point, geometrically necessary dislocations (GND) are generated at the soft phase and interface to adapt to this deformation compatibility [42]. The stress concentration at the interface can induce stress−strain relaxation, which subsequently contributes to an elevated proportion of interfacial segregation in WHEAs. This phenomenon makes the observation of tungsten cleavage after fracture more challenging. Additionally, it may be related to the poorer wettability of HEA in tungsten and the impact of Cr−Mn oxides, which weakens the interfacial bond.

At 1400 °C, the dominant fracture mode is W−W interface separation, primarily attributed to inadequate diffusion and distribution of the binder. With increasing temperature, the contact between the binder and W particles is more extensive, leading

to noticeable W−binder separation and even some tungsten cleavage (Fig. 7(b)), which further supports the superior mechanical properties observed at 1450 °C. As the temperature continues to rise, the grain is larger and the C_W of the alloy increases. Consequently, the fracture mode shifts towards the detachment of the W−binder and W−W interface, while the oxide particles experience significant growth, collectively contributing to a substantial weakening of the material performance.

Figure 8(a) displays the hardness of sintered blocks. The overall hardness fluctuates around HV 400 and exhibits a slight increase with rising temperature. The micrometer scale hardness tester used here provides an assessment of the collective hardness of tungsten and other constituent phases. The overall hardness can be calculated using the following formula [15]:

$$H_{total}=H_W V_S+H_B V_B+H_O V_O \quad (9)$$

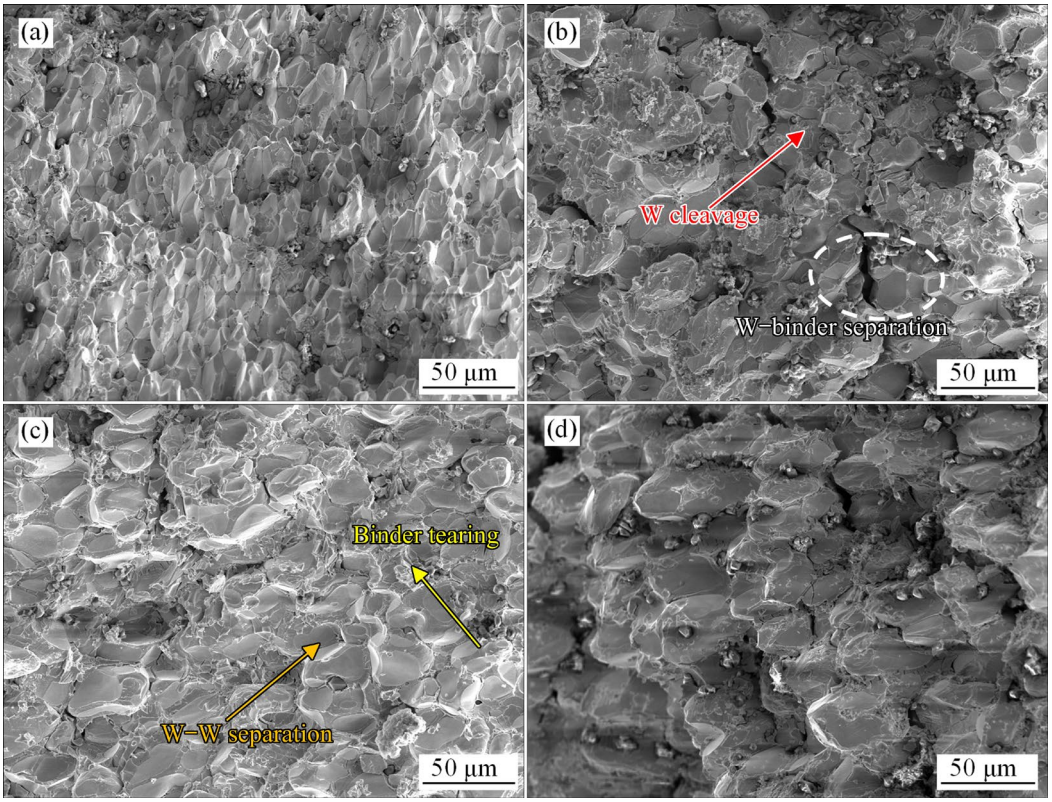

Fig. 7 Fracture morphologies of 95W-HEA samples sintered at different temperatures: (a) 1400 °C; (b) 1450 °C; (c) 1500 °C; (d) 1550 °C

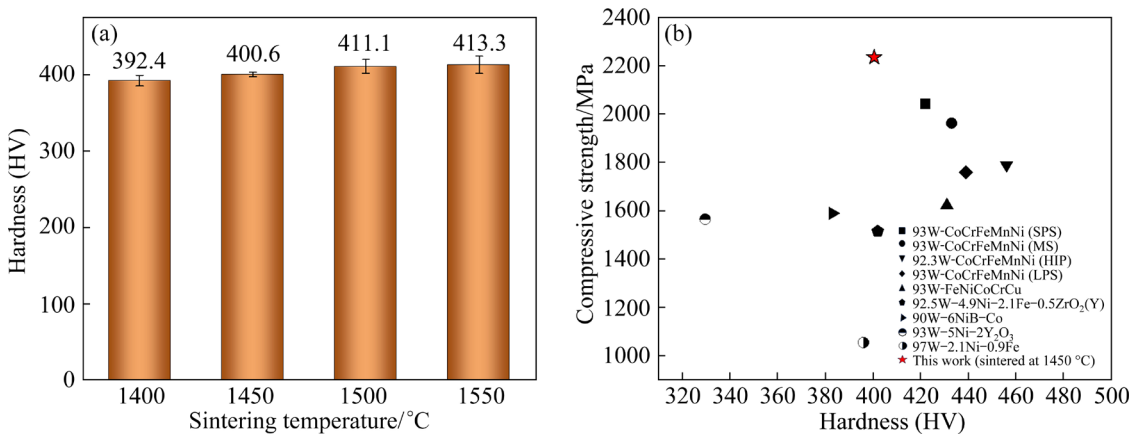

Fig. 8 (a) Hardness of samples at different sintering temperatures and (b) comparison of mechanical properties with other literature

where H_W, H_B and H_O represent the hardness of the tungsten, binder and Cr−Mn oxide, respectively, while V_S, V_B and V_O represent their phase volume fraction.

In Table 2, the volume fraction of the tungsten phase (V_S) is tested with the highest proportion in the alloys. It can be concluded that a slight increase in V_S brings about a mild increase in hardness, within the margin of error. That is to say, the hardness increase is caused by the more tungsten content in the hardness test area. Our findings surpass the performance of traditional Ni−Fe systems and certain HEA binders [15,20,43−47], as shown in Fig. 8(b). This superiority is primarily attributed to the high tungsten content and the utilization of an HEA binder phase.

4 Conclusions

(1) The sintering temperature has a significant impact on the relative density, grain size, W−W contiguity, and mechanical properties of the 95W-HEA alloys. As the sintering temperature increases, the elative density and grain size of alloy increase. The compressive strength initially increases, then decreases, and the contiguity shows the inverse trend.

(2) At a sintering temperature of 1450 °C, the sample with the optimal performance was prepared, exhibiting a density of 96.61%, a W−W contiguity of 0.53, an average grain size of 18.97 μm, a compressive strength of 2234.82 MPa, and a hardness of HV 400.6.

(3) The microstructure of the 95W-HEA alloys consists of a W phase, a γ(W,Ni,Fe,Co) HEA phase, and a mixed Cr−Mn oxide phase.

(4) The liquid phase activation energy of tungsten using the CoCrFeMnNi HEA as a binder is 354.514 kJ/mol, significantly higher than that of conventional Ni−Fe and Ni−Co binders. This suggests that tungsten grain growth in this HEA binder is more challenging.

(5) Under compression loading, the 95W-HEA alloy tends to exhibit brittle fracture due to the detachment of the W−binder, W−W interface, and tearing of binder.

CRediT authorship contribution statement

Shi-dong XIE: Investigation, Data curation, Writing − Original draft, Formal analysis; **Liang-liang TANG:** Investigation, Validation, Resources; **Bo-hua DUAN:** Conceptualization, Project administration, Methodology, Supervision, Writing − Review & editing; **Zhuang-zhi WU:** Supervision, Resources, Writing − Review & editing; **De-zhi WANG:** Supervision, Resources, Writing − Review & editing.

Declaration of competing interest

The authors declare that they have no known competing financial interests or personal relationships that could have appeared to influence the work reported in this paper.

Acknowledgments

This work was supported by the National Natural Science Foundation of China (No. 51874368).

References

[1] UPADHYAYA A. Processing strategy for consolidating tungsten heavy alloys for ordnance applications [J]. Materials Chemistry and Physics, 2001, 67(1): 101−110.

[2] NEU R, MAIER H, BALDEN M, ELGETI S, GIETL H, GREUNER H, HERRMANN A, HOUBEN A, ROHDE V, SIEGLIN B, ZAMMUTO I. Investigations on tungsten heavy alloys for use as plasma facing material [J]. Fusion Engineering and Design, 2017, 124: 450−454.

[3] SENTHILNATHAN N, RAJA ANNAMALAI A, VENKATACHALAM G. Sintering of tungsten and tungsten heavy alloys of W−Ni−Fe and W−Ni−Cu: A review [J]. Transactions of the Indian Institute of Metals, 2017, 70(5): 1161−1176.

[4] KUMARI A, SANKARANARAYANA M, NANDY T K. On structure property correlation in high strength tungsten heavy alloys [J]. International Journal of Refractory Metals and Hard Materials, 2017, 67: 18−31.

[5] GERMAN R M. Sintered tungsten heavy alloys: Review of microstructure, strength, densification, and distortion [J]. International Journal of Refractory Metals and Hard Materials, 2022, 108: 105940.

[6] LUO R, HUANG D, YANG M, TANG E, WANG M, HE L. Penetrating performance and “self-sharpening” behavior of fine-grained tungsten heavy alloy rod penetrators [J]. Materials Science and Engineering A, 2016, 675: 262−270.

[7] ZHANG X H, ZHU S J, ZHANG B, AHMAD T, WANG C M, ZHOU L L, LIANG T X, YANG B. Effect of Y_2O_3 addition on the microstructure, wear Resistance, and corrosion behavior of W−4.9Ni−2.1Fe heavy alloy [J]. Journal of Materials Engineering and Performance, 2019, 28: 4801−4810.

[8] MANIKANDAN R, RAJA ANNAMALAI A. Effect of Mn addition in W−Ni−Cu heavy alloy processed through hot press sintering techniques on microstructure, microtexture and grain boundary character evolution [J]. Materials Characterization, 2024, 210: 113808.

[9] DUAN B H, ZHOU T, YANG G, YANG D L, WANG D Z. Microstructures and properties of 90W−4Ni−6Mn alloy

prepared by vacuum sintering [J]. Materials Research Express, 2020, 7(3): 36522.

[10] MIRACLE D B, SENKOV O N. A critical review of high entropy alloys and related concepts [J]. Acta Materialia, 2017, 122: 448−511.

[11] KRISHNA S A, NOBLE N, RADHIKA N, SALEH B. A comprehensive review on advances in high entropy alloys: Fabrication and surface modification methods, properties, applications, and future prospects [J]. Journal of Manufacturing Processes, 2024, 109: 583−606.

[12] KAREEM S A, ANAELE J U, AIKULOLA E O, ADEWOLE T A, BODUNRIN M O, ALANEME K K. Design and selection of metal matrix composites reinforced with high entropy alloys−Functionality appraisal and applicability in service: A critical review [J]. Journal of Alloys and Metallurgical Systems, 2024, 5: 100057.

[13] JIAN R Z, WANG L, ZHOU S C, ZHU Y C, LIANG Y, WANG B P, XUE Y F. Achieving fine-grain tungsten heavy alloys by selecting a high entropy alloy matrix with low W grain growth rate [J]. Materials Letters, 2020, 278: 128405.

[14] ZHOU S C, JIAN R Z, LIANG Y, ZHU Y C, WANG B P, WANG L, WANG L, REN Y, XUE Y F. High susceptibility to adiabatic shear banding and high dynamic strength in tungsten heavy alloys with a high-entropy alloy matrix [J]. Journal of Alloys and Compounds, 2021, 859: 157796.

[15] PANIGRAHI A, ACHARYA T S, SENGUPTA P, KUMAR D, SARANGI L, KUMAR N, DEBASISH D, SUWAS S, BASU S, DEBATA M. Microstructure and mechanical properties of novel tungsten heavy alloys prepared using FeNiCoCrCu HEA as binder [J]. Materials Science and Engineering A, 2022, 832: 142451.

[16] LI Z B, ZHANG G H, CHOU K C. Simultaneous enhancements of strength and hardness for fine-grained W-NiFeCoCrMn composites [J]. Materials Characterization, 2023, 201: 112933.

[17] CHEN H, LI D, GENG Z W, WU Y Y, ZHANG T M, JIANG X, ZHAO S, ZHANG H, HAN Y, LIU X, CHEN C. Additive manufactured high-strength tungsten composite with high deformability by using a novel CoCrNi medium-entropy binder [J]. Composites Part B: Engineering, 2022, 246: 110256.

[18] LIU W S, MA Y Z, ZHANG J J. Properties and microstructural evolution of W−Ni−Fe alloy via microwave sintering [J]. International Journal of Refractory Metals & Hard Materials, 2012, 35: 138−142.

[19] SENTHILNATHAN N, ANNAMALAI A R, VENKATACHALAM G. Microstructure and mechanical properties of spark plasma sintered tungsten heavy alloys [J]. Materials Science and Engineering A, 2018, 710: 66−73.

[20] SATYANARAYANA P V, SOKKALINGAM R, JENA P K, SIVAPRASAD K, PRASHANTH K G. Tungsten matrix composite reinforced with CoCrFeMnNi high-entropy alloy: Impact of processing routes on microstructure and mechanical properties [J]. Metals (Basel), 2019, 9(9): 992.

[21] SUDHA G T, STALIN B, RAVICHANDRAN M, BALASUBRAMANIAN M. Mechanical properties, characterization and wear behavior of powder metallurgy composites—A Review [J]. Materials Today: Proceedings, 2020, 22: 2582−2596.

[22] CANTOR B, CHANG I T H, KNIGHT P, VINCENT A J B. Microstructural development in equiatomic multicomponent alloys [J]. Materials Science and Engineering A, 2004, 375/376/377: 213−218.

[23] YANG X, ZHANG Y. Prediction of high-entropy stabilized solid-solution in multi-component alloys [J]. Materials Chemistry and Physics, 2012, 132(2): 233−238.

[24] GUO S, NG C, LU J, LIU C T. Effect of valence electron concentration on stability of FCC or BCC phase in high entropy alloys [J]. Journal of Applied Physics, 2011, 109(10): 103505.

[25] LI Z B, WANG Y, ZHANG H, CHEN B, ZHANG G H, CHOU K C. Effect of ZrB_2 addition on microstructure evolution and mechanical properties of 93 wt.% tungsten heavy alloys [J]. Materials Science and Engineering A, 2021, 825: 141870.

[26] XIE Y H, ZHOU D S, LUO Y F, XIA T, ZENG W, LI C G, WANG J, LIANG J M, ZHANG D. Fabrication of CoCrFeNiMn high entropy alloy matrix composites by thermomechanical consolidation of a mechanically milled powder [J]. Materials Characterization, 2019, 148: 307−316.

[27] VAIDYA M, TRUBEL S, MURTY B S, WILDE G, DIVINSKI S V. Ni tracer diffusion in CoCrFeNi and CoCrFeMnNi high entropy alloys [J]. Journal of Alloys and Compounds, 2016, 688: 994−1001.

[28] GERMAN R M, SURI P, PARK S J. Review: Liquid phase sintering [J]. Journal of Materials Science, 2009, 44(1): 1−39.

[29] LUO J, GUPTA V K, YOON D H, MEYER H M. Segregation-induced grain boundary premelting in nickel-doped tungsten [J]. Applied Physics Letters, 2005, 87(23): 231902.

[30] CANTWELL P R, TANG M, DILLON S J, LUO J, ROHRER G S, HARMER M P. Grain boundary complexions [J]. Acta Materialia, 2014, 62: 1−48.

[31] HU K, LI X Q, AI X, QU S G, LI Y Y. Fabrication, characterization, and mechanical properties of 93W−4.9Ni−2.1Fe/95W−2.8Ni−1.2Fe−1Al_2O_3 heavy alloy composites [J]. Materials Science and Engineering A, 2015, 636: 452−458.

[32] LI Z B, YANG X H, ZHANG G H, CHOU K C. Realizing excellent strength-ductility synergy in ultrafine-grained medium W content composites reinforced with multiple strengthening mechanisms [J]. Materials Science and Engineering A, 2023, 885: 145583.

[33] LIU J X, UPADHYAYA A, GERMAN R M. Application of percolation theory in predicting shape distortion during liquid-phase sintering [J]. Metallurgical and Materials Transactions. A: Physical Metallurgy and Materials Science, 1999, 30(8): 2209−2220.

[34] LIU J X, GERMAN R M. Microstructural parameters related to liquid-phase sintering [J]. Metallurgical and Materials Transactions A: Physical Metallurgy and Materials Science, 2000, 31(10): 2607−2614.

[35] PANCHAL A, VENUGOPAL REDDY K, AZEEM P A, SARKAR R, PARADKAR A, NANDY T K, SINGH A K. Effect of Ni/Fe ratio on microstructure, tensile flow and work hardening behaviour of tungsten heavy alloys in heat treated and swaged conditions [J]. Philosophical Magazine (Abingdon, England), 2021, 101(2): 211−241.

[36] VOORHEES P W, GLICKSMAN M E. Ostwald ripening

during liquid phase sintering−Effect of volume fraction on coarsening kinetics [J]. Metallurgical Transactions A: Physical Metallurgy and Materials Science, 1984, 15A(6): 1081−1088.

[37] PARK S J, MARTIN J M, GUO J F, JOHNSON J L, GERMAN R M. Grain growth behavior of tungsten heavy alloys based on the master sintering curve concept [J]. Metallurgical and Materials Transactions A: Physical Metallurgy and Materials Science, 2006, 37(11): 3337−3346.

[38] MA H, SHAO Y, SHEK C H. Microstructure, grain growth behavior and mechanical properties of W-CoCuFeNi tungsten heavy alloys prepared by infiltration [J]. International Journal of Refractory Metals and Hard Materials, 2021, 98: 105572.

[39] LEE K H, CHA S I, RYU H J, HONG S H. Effect of oxide dispersoids addition on mechanical properties of tungsten heavy alloy fabricated by mechanical alloying process [J]. Materials Science and Engineering A, 2007, 452: 55−60.

[40] LI Z, ZHANG H, ZHANG G, CHOU K. Superior strength-ductility synergy in a novel tailored Zr-based particle-strengthened medium W content alloys [J]. Composites Part B: Engineering, 2022, 236: 109817.

[41] SATHIYAMOORTHI P, KIM H S. High-entropy alloys with heterogeneous microstructure: Processing and mechanical properties [J]. Progress in Materials Science, 2022, 123: 100709.

[42] SU X W, HE Z, YIN T, YAN S X, HOU Y T, MAO H, LI M Y, DONG L L, SUN G, ZHANG Y. Fine-grained 93W−4.9Ni−2.1Fe alloy with ultrahigh yield strength prepared via low temperature sintering of W nanocomposite powder [J]. Materials Science and Engineering A, 2023, 879: 145298.

[43] ANWER Z, UMER M A, NISAR F, HAFEEZ M A, YAQOOB K, LUO X, AHMAD I. Microstructure and mechanical properties of hot isostatic pressed tungsten heavy alloy with FeNiCoCrMn high entropy alloy binder [J]. Journal of Materials Research and Technology, 2023, 22: 2897−2909.

[44] XU L J, XIAO F N, WEI S Z, ZHOU Y C, PAN K M, LI X Q, LI J W, LIU W. Development of tungsten heavy alloy reinforced by cubic zirconia through liquid-liquid doping and mechanical alloying methods [J]. International Journal of Refractory Metals and Hard Materials, 2019, 78: 1−8.

[45] SENGUPTA P, MEHER P, PANIGRAHI A, MANDAL S, BASU S, DEBATA M. Microstructure, distortion characteristics and mechanical behaviour of NiB modified 90W-6Ni-4Co heavy alloys [J]. Journal of Alloys and Compounds, 2021, 887: 161404.

[46] DAOUSH W M R, ELSAYED A H A, KADY O A G E, SAYED M A, DAWOOD O M. Enhancement of physical and mechanical properties of oxide dispersion-strengthened tungsten heavy alloys [J]. Metallurgical and Materials Transactions A: Physical Metallurgy and Materials Science, 2016, 47(5): 2387−2395.

[47] LI Z B, ZHANG H, ZHANG G H, CHOU K C. Fabrication and characterization of tungsten heavy alloys with high W content by powder metallurgy [J]. Metallurgical and Materials Transactions A: Physical Metallurgy and Materials Science, 2022, 53(3): 1085−1098.

烧结温度对 95W-HEA 合金显微组织和力学性能的影响

谢世冬，唐亮亮，段柏华，吴壮志，王德志

中南大学 材料科学与工程学院，长沙 410083

摘　要：高熵合金作为钨基高比重合金的黏结剂展现了潜在的优势。采用粉末冶金方法在 1400~1550 ℃烧结制备了 95W-5CoCrFeMnNi (95W-HEAs)合金。显微组织分析表明，95W-HEAs 中钨相呈现近球形形貌并嵌在 HEA 黏结剂基质中，并出现 Cr−Mn 氧化物混合相。烧结温度对合金的相对密度、晶粒尺寸、W−W 连接度和力学性能有显著影响。在 1450 ℃烧结的 95W-HEAs 合金获得了最优的综合性能，其相对密度为 96.61%、W−W 连接度为 0.528、平均晶粒尺寸为 18.97 μm、抗压强度为 2234.82 MPa、硬度为 HV 400.6。计算出钨在 HEA 黏结剂形成的液相中扩散激活能为 354.514 kJ/mol，突出了 HEA 黏结剂对晶粒生长的控制作用。

关键词：钨基高比重合金；高熵合金黏结剂；烧结温度；致密化；力学性能

(Edited by Bing YANG)